Appl. Phys. B 91, 249–256 (2008)
DOI: 10.1007/s00340-008-2981-y

Applied Physics B
Lasers and Optics

M. EICHHORN[1,✉]
S.T. FREDRICH-THORNTON[2]
E. HEUMANN[2]
G. HUBER[2]

Spectroscopic properties of Er^{3+}:YAG at 300–550 K and their effects on the 1.6 μm laser transitions

[1] French-German Research Institute of Saint-Louis (ISL), 5 rue du Général Cassagnou, BP 70034, 68301 Saint Louis Cedex, France
[2] Institut für Laser-Physik (ILP), Universität Hamburg, Luruper Chaussee 149, 22761 Hamburg, Germany

Received: 12 February 2008
Published online: 27 March 2008 •

ABSTRACT The temperature dependent lifetimes, absorption, and emission spectra of an Er^{3+}:YAG at 300–550 K are investigated and compared to the expected evolution using a theoretical description of the spectra. Population and linewidth dependent changes in the spectra can be separated, allowing conclusions on pump and laser efficiency at elevated temperatures. The temperature sensitivity of Er^{3+}:YAG is for instance much less than that of Yb^{3+}:YAG.

PACS 42.55.Rz; 78.00.00; 78.47.-p; 42.70.Hj

1 Introduction

Er^{3+}:YAG is an interesting laser material for eye-safe emission at wavelengths of 1617 and 1645 nm which can be resonantly diode-pumped into the upper laser manifold at 1475 and 1532 nm [1, 2]. Due to the low quantum defect high slope efficiencies of $> 80\%$ have been achieved with direct fiber laser pumping [3]. Recent research has focused on cryogenic cooling of Er^{3+}:YAG to enhance spectroscopic emission cross-section and thermal conductivity [4] for high energy laser applications. However, the desired spectral narrowing of the emission lines at cryogenic temperatures also narrows the absorption lines and has therefore a detrimental effect on pump absorption. Here, a spectroscopic analysis of Er^{3+}:YAG at elevated temperatures of 300–550 K is presented, that are easily reached in several laser architectures. In order to gain a deeper insight into the processes governing the temperature dependence of the spectra, the absorption and emission spectra relating to the ${}^4I_{15/2} \leftrightarrow {}^4I_{13/2}$ transitions were analyzed using a theory based on the spectroscopic Debye temperature. With these simulated spectra the temperature influence on the laser performance is numerically investigated and the results indicate that efficient lasing should be possible even above 500 K.

✉ Fax: +33-389-69-5077, E-mail: Marc.Eichhorn@isl.eu

2 Spectral theory

The spectral theory described here is based on a decomposition of the measured spectra into the different transition lines. Each line is then treated as temperature dependent using a simple approach derived from the interaction between the erbium ions and the crystal field.

The greatest influence of temperature on the spectra is due to the thermal population of the different levels. But also the lineshapes and line-positions will change with temperature. To model this adequately, the Boltzmann occupation of the levels is included into the total spectroscopic cross-sections for absorption ($\sigma_\mathrm{a}(\lambda)$) and emission $\sigma_\mathrm{e}(\lambda)$. They are related to the intrinsic atomic cross-sections $\sigma_{ij}(\lambda)$ by [5],

$$\sigma_\mathrm{a}(\lambda) = \sum_{ij} d_i \frac{\mathrm{e}^{-\frac{E_{g,i}}{k_\mathrm{B}T}}}{Z_g} \sigma_{ij}(\lambda) d_j \,, \tag{1}$$

$$\sigma_\mathrm{e}(\lambda) = \sum_{ij} d_j \frac{\mathrm{e}^{-\frac{E_{u,j}}{k_\mathrm{B}T}}}{Z_u} \sigma_{ji}(\lambda) d_i \,. \tag{2}$$

Therein, $E_{g,i}$ and $E_{u,j}$ are the energies of the levels in the lower and upper manifold, respectively, d_i and d_j their degeneracies and Z_g and Z_u the corresponding partition functions.

The measured absorption and emission cross-sections at temperature T_0 can be decomposed into a sum of Lorentzian lines

$$\sigma_\mathrm{a}(\lambda, T_0) = \sum_{ij} \sigma_{\mathrm{a},ij}(\lambda, T_0) \,, \tag{3}$$

$$\sigma_\mathrm{e}(\lambda, T_0) = \sum_{ij} \sigma_{\mathrm{e},ij}(\lambda, T_0) \,, \tag{4}$$

with

$$\sigma_{\mathrm{a},ij}(\lambda, T_0) = \frac{2A^\mathrm{a}_{ij}(T_0)}{\pi} \frac{w^\mathrm{a}_{ij}(T_0)}{4(\lambda - \lambda^\mathrm{a}_{ij}(T_0))^2 + w^\mathrm{a}_{ij}(T_0)^2} \,, \tag{5}$$

$$\sigma_{\mathrm{e},ij}(\lambda, T_0) = \frac{2A^\mathrm{e}_{ij}(T_0)}{\pi} \frac{w^\mathrm{e}_{ij}(T_0)}{4(\lambda - \lambda^\mathrm{e}_{ij}(T_0))^2 + w^\mathrm{e}_{ij}(T_0)^2} \,, \tag{6}$$

being the corresponding Lorentzian functions. Therein $A_{ij}^{\mathrm{a/e}}(T_0)$ is the line area, given by

$$A_{ij}^{\mathrm{a/e}}(T_0) = \int \sigma_{\mathrm{a/e},ij}(\lambda, T_0)\,\mathrm{d}\lambda\,, \tag{7}$$

where $w_{ij}(T_0)$ the full width at half maximum and $\lambda_{ij}(T_0)$ the peak position. It will be later demonstrated that the line area depends only on the thermal population of the level while the width and peak positions are temperature dependent due to the ion-host interactions and can be described by simple functions. By comparing (1) and (2) with (3) and (4), the intrinsic atomic cross-sections can be unambiguously related to the different measured lines and then the spectroscopic absorption cross-section

$$\sigma_{\mathrm{a}}(\lambda, T) = \sum_{ij} \frac{f_{g,i}(T)}{f_{g,i}(T_0)} \sigma_{\mathrm{a},ij}(\lambda - \lambda_{ij}^{\mathrm{a}}(T), w_{ij}^{\mathrm{a}}(T), A_{ij}^{\mathrm{a}}(T_0)) \tag{8}$$

can be determined for all temperatures T in the range of 300–550 K and beyond. As can be shown, there is also an equivalent expression for the emission cross-section

$$\sigma_{\mathrm{e}}(\lambda, T) = \sum_{ij} \frac{f_{u,j}(T)}{f_{u,j}(T_0)} \sigma_{\mathrm{e},ij}(\lambda - \lambda_{ij}^{\mathrm{e}}(T), w_{ij}^{\mathrm{e}}(T), A_{ij}^{\mathrm{e}}(T_0))\,, \tag{9}$$

in which

$$f_{g,i}(T) = \frac{d_i}{Z_g} \mathrm{e}^{-\frac{E_{g,i}}{k_{\mathrm{B}}T}}\,, \tag{10}$$

$$f_{u,j}(T) = \frac{d_j}{Z_u} \mathrm{e}^{-\frac{E_{u,j}}{k_{\mathrm{B}}T}}\,, \tag{11}$$

are the Boltzmann occupation factors of the Stark levels.

The temperature dependence of the linewidths for $T > 180$ K is dominated by two-phonon Raman scattering [6], which is a homogeneous process. This explains why the cross-sections could accurately be fitted by Lorentzian lines. In general the width of a level can be described by [6–10]

$$\Delta\nu(T) = \Delta\nu_0 + \Delta\nu_{\mathrm{D}}(T) + \Delta\nu_{\mathrm{R}}(T)\,, \tag{12}$$

wherein $\Delta\nu_0$ takes account for the temperature independent processes as e.g. statistical strain distributions. $\Delta\nu_{\mathrm{D}}(T)$ corresponds to the direct emission or absorption of a phonon and $\Delta\nu_{\mathrm{R}}(T)$ represents the two-phonon Raman scattering. The direct process can be neglected here as it only contributes at low temperatures. To model the linewidths, the Raman process can be described by

$$\Delta\nu_{\mathrm{R}}(T) = a_1 f_{\mathrm{R}}(T)\,, \tag{13}$$

with

$$f_{\mathrm{R}}(T) = \left(\frac{T}{\Theta_{\mathrm{S}}}\right)^7 \int_0^{\frac{\Theta_{\mathrm{S}}}{T}} \frac{x^6 \mathrm{e}^x}{(\mathrm{e}^x - 1)^2}\,\mathrm{d}x \tag{14}$$

and a transition dependent parameter a_1 [7]. Θ_{S} is the spectroscopic Debye temperature, which was measured in low-doped Er^{3+}:YAG as $\Theta_{\mathrm{S}} = 405$ K [6]. The spectroscopic Debye temperature is not identical to the Debye temperature describing heat capacity as not all phonons couple to the ionic levels.

The level positions are treated equivalently, calculated from the temperature-dependent level shift. This level shift is caused by the interaction of the ion with the crystal field of the host, which itself depends on the local strain in the crystal. This level shift can be written as [6–10]

$$\Delta E(T) = \Delta E_0 + \Delta E_{\mathrm{D}}(T) + \Delta E_{\mathrm{R}}(T)\,. \tag{15}$$

The direct process $\Delta E_{\mathrm{D}}(T)$ can often be neglected as usually the levels are well separated and so no coupling occurs between them. Therefore, the level shift is dominated by the Raman process, which is given by

$$\Delta E_{\mathrm{R}}(T) = a_2 g_{\mathrm{R}}(T)\,, \tag{16}$$

with

$$g_{\mathrm{R}}(T) = \left(\frac{T}{\Theta_{\mathrm{S}}}\right)^4 \int_0^{\frac{\Theta_{\mathrm{S}}}{T}} \frac{x^3}{\mathrm{e}^x - 1}\,\mathrm{d}x \tag{17}$$

and a_2 is a transition dependent parameter [7]. In this way the different energy levels needed, e.g., to calculate the temperature dependent partition functions of the $^4I_{15/2}$ and $^4I_{13/2}$ manifolds can be derived using

$$E_i(T) = E_{i,0} + (E_i(T_0) - E_{i,0}) \frac{g_{\mathrm{R}}(T)}{g_{\mathrm{R}}(T_0)} \tag{18}$$

and the line positions are calculated by

$$\frac{1}{\lambda_{ij}(T)} = \frac{1}{\lambda_{ij,0}} + \left(\frac{1}{\lambda_{ij}(T_0)} - \frac{1}{\lambda_{ij,0}}\right) \frac{g_{\mathrm{R}}(T)}{g_{\mathrm{R}}(T_0)}\,. \tag{19}$$

As the widths of the levels involved in a transition simply add for homogeneous broadening, the linewidth $w_{ij}(T)$ of the transition can be described accurately for temperatures $T > 180$ K by

$$w_{ij}(T) = w_{ij,0} + (w_{ij}(T_0) - w_{ij,0}) \frac{f_{\mathrm{R}}(T)}{f_{\mathrm{R}}(T_0)}\,. \tag{20}$$

The temperature dependence of the factors $f_{\mathrm{R}}(T)$ and $g_{\mathrm{R}}(T)$ is depicted in Fig. 1. In the presented theory, it is important that the Lorentzian functions used in the (5) and (6) have constant integrals, independent of $w_{ij}(T)$. Thus the normalization generates the correct peak values of the lines.

3 Spectroscopic measurements and results

3.1 *Lifetimes*

Fluorescence lifetimes were measured using a pulsed optical-parametric oscillator exciting an 0.5% Er^{3+}:YAG sample at 963 nm. The fluorescence was then filtered through a 0.5 m monochromator and detected by a photomultiplier. The monochromator wavelength (detected fluorescence) was 1532 and 1006 nm for the $^4I_{13/2}$ and $^4I_{11/2}$ manifold, respectively.

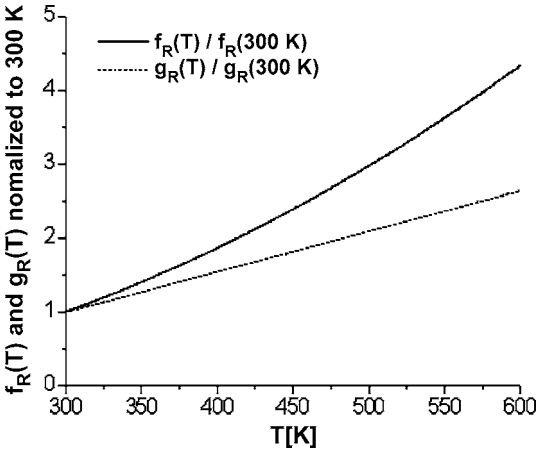

FIGURE 1 Raman scaling factors for linewidth and line positions

For the $^4I_{13/2}$ manifold the measured fluorescence lifetimes are nearly temperature independent, plotted in Fig. 2. Using the radiative transition lifetime of the $^4I_{13/2}$ manifold of $\tau_{sp} = 8.25$ ms [11], the expected multiphonon relaxation influence agrees reasonably with the values found in the range 300–500 K. The fluorescence lifetime τ_f can be derived from the radiative lifetime τ_{sp} and the multiphonon relaxation lifetime τ_r as [12]

$$\frac{1}{\tau_f} = \frac{1}{\tau_{sp}} + \frac{1}{\tau_r} = \frac{1}{\tau_{sp}} + \frac{W_0}{\left(1 - e^{-\frac{E_P}{k_B T}}\right)^{n_P}} . \tag{21}$$

Therein $W_0 = 8.198\,s^{-1}$ and $\tau_r(300\,K) = 103$ ms were determined by taking the difference between $\tau_f(300\,K) = 7.64$ ms and τ_{sp} at 300 K, using an effective phonon energy of $E_P = 782\,cm^{-1}$ and an effective phonon number of $n_P = 8$ [12]. Regarding this large effective phonon number as well as the fact that the predicted multiphonon relaxation curve in Fig. 2 does not exactly fit to the data points in terms of curvature, it seems possible that the temperature dependence of the lifetime of the $^4I_{13/2}$ manifold may not be dominated by multiphonon relaxation and that another effect is responsible for the drop in lifetime. This effect may be related to temperature dependent changes in the crystal field.

The fluorescence lifetime of the $^4I_{13/2}$ manifold corresponds to a quantum yield of 92.5% at room temperature and leads to two important conclusions: First the multiphonon relaxation of the $^4I_{13/2}$ manifold is weak even at elevated temperatures, conserving the high quantum yield of the laser. Second the spontaneous lifetime of the $^4I_{13/2}$ manifold is temperature independent. Since spontaneous lifetime and integrated emission cross-section is coupled by

$$\tau_{sp} = \frac{1}{8\pi n^2 c \int \frac{\sigma_e(\lambda)}{\lambda^4}\,d\lambda} , \tag{22}$$

and the different lines in the spectra are narrow compared to their absolute line position, the integral over the emission cross-section of a line is a constant. As emission and absorption are connected by reciprocity, a constant line area also follows for an absorption line. This makes the detailed theoretical description of the temperature-dependent cross-sections in Sect. 2 possible.

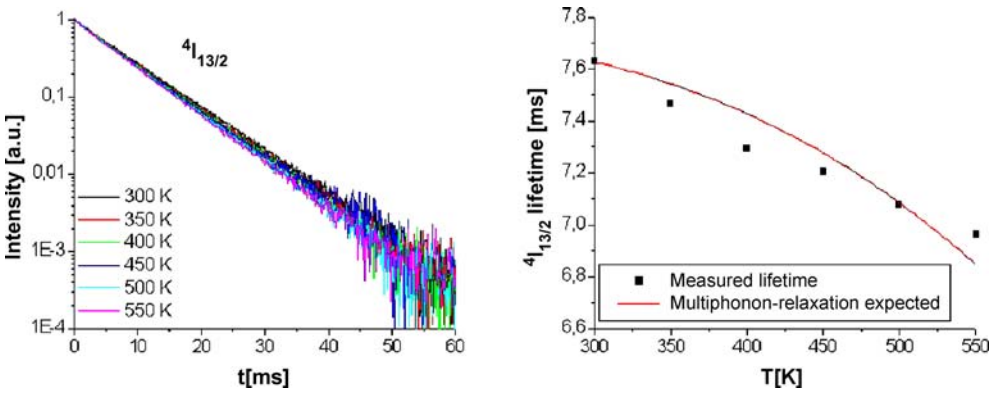

FIGURE 2 Measured lifetimes and expected multiphonon relaxation for the $^4I_{13/2}$ manifold

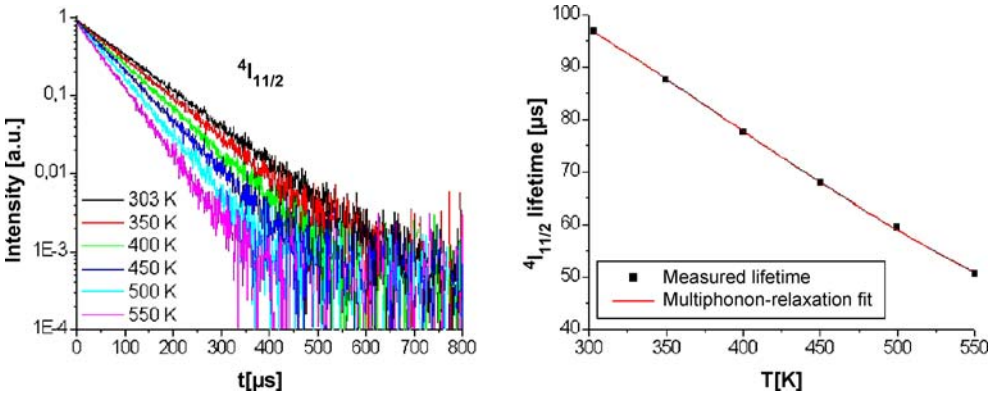

FIGURE 3 Measured lifetimes and derived multiphonon relaxation for the $^4I_{11/2}$ manifold

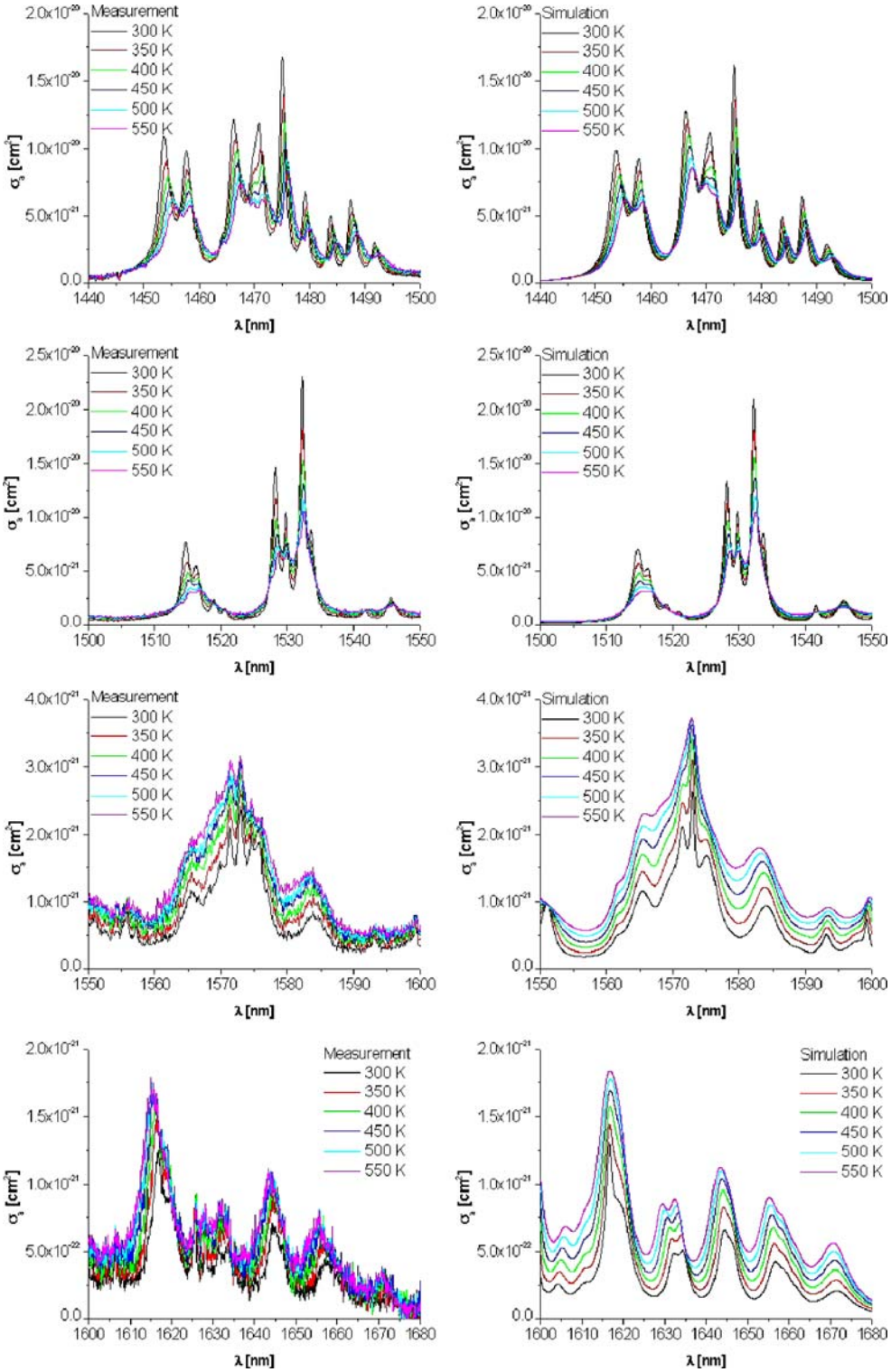

FIGURE 4 Measured (*left*) and simulated (*right*) absorption cross-section

The fluorescence lifetime of the $^4I_{11/2}$ manifold changes from 97 µs at 300 K approximately linearly to 50 µs at 550 K. A fit of (21) to the measured data in Fig. 3 shows that the multiphonon transition rate of the $^4I_{11/2}$ manifold can be described by $E_P = 712\,\mathrm{cm}^{-1}$, an effective phonon number of $n_P = 4.85$ and a spontaneous transition rate of $W_0 = 8615\,\mathrm{s}^{-1}$.

3.2 *Cross-sections*

The spectroscopic measurements were performed on a 5 mm cube of uncoated 0.5% Er^{3+}:YAG placed in a resistive oven for temperature control. A 1 m grating spectrometer and cooled InGaAs photodiodes were used to record the spectra, resulting in a resolution of 0.32 nm. Absorption was

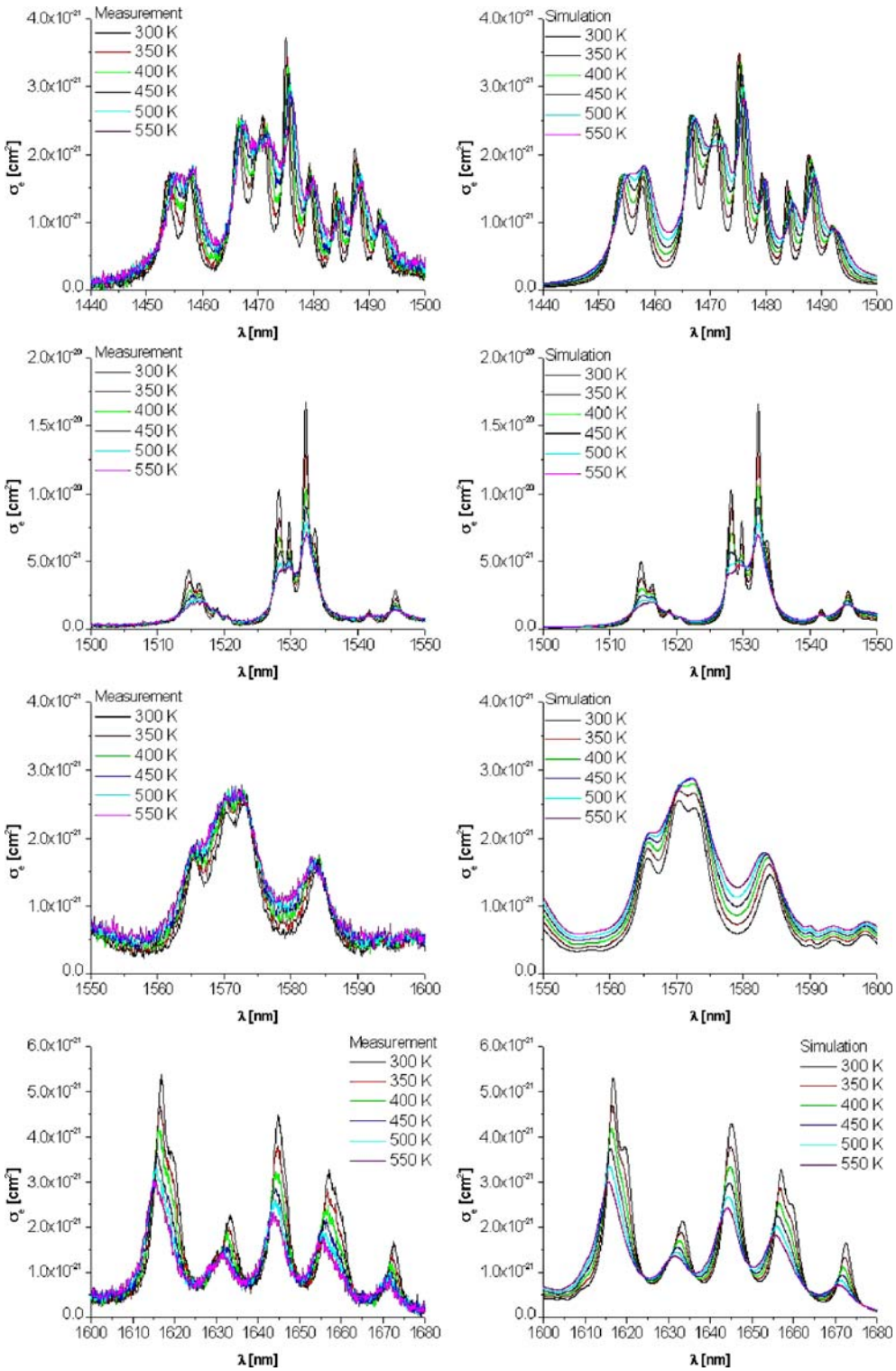

FIGURE 5 Measured (*left*) and simulated (*right*) emission cross-section

measured with a broadband halogen lamp and emission via excitation to the $^4I_{11/2}$ manifold using a Ti:sapphire laser at 963.3 nm.

4 Discussion

The measured absorption and emission spectra in the range 300–550 K could be accurately reproduced using the corresponding measured 300 K spectrum and the spectral theory described in Sect. 2. As can be seen in Figs. 4 and 5 the calculated spectra agree well with the experimental data for individual lines that do not overlap much with others, as well as for the wavelengths where many different lines overlap, i.e. where it is difficult to separate the temperature dependent evolution for the different lines.

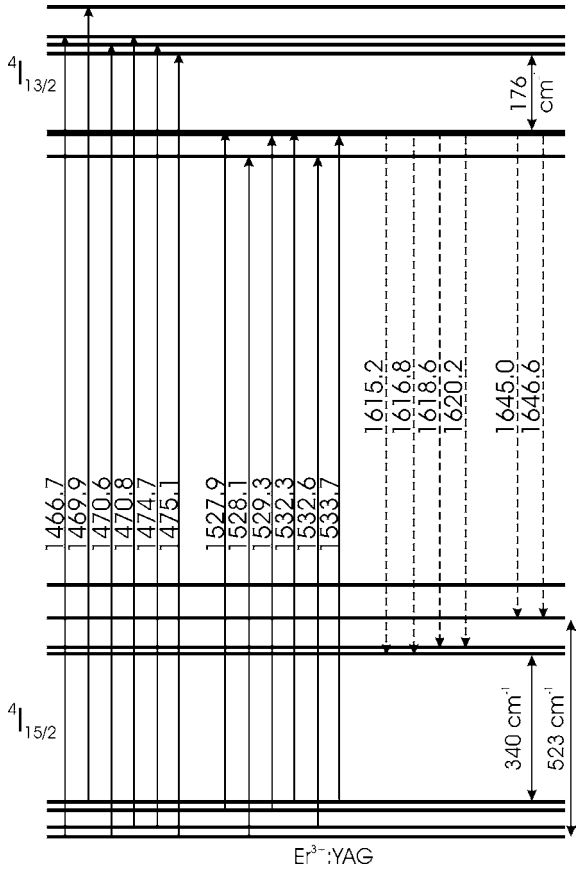

FIGURE 6 Level diagram of Er^{3+}:YAG and its most important lines (wavelength in nm at 300 K)

4.1 *Absorption*

The absorption lines of greatest interest for direct diode pumping are those at around 1475 nm and 1532 nm, as can be seen in Fig. 4. All these lines start from the first four Stark levels in the ground state manifold at 0, 18, 58 and 75 cm^{-1}, building a sub-manifold, see Fig. 6. Due to their close energetic positions and the fact that the other four levels of the ground state manifold, the second sub-manifold, are at least separated by 340 cm^{-1} from the lower sub-manifold, thermodynamic calculations using (10) and (11) demonstrate that between 300 and 600 K 86%–78% of the total population of the $^4I_{15/2}$ manifold occupy the lowest four energy levels. Thus thermal depopulation of the absorption levels is no significant process in Er^{3+}:YAG.

4.1.1 Pumping around 1475 nm. High power laser diodes are available at this wavelength. As these diodes show broad emission linewidths of up to 15 nm, they are optimally suited for pumping this broad absorption band. The only drawback of this approach is the increased crystal heat load of 10.3% compared to 6.9% for 1532 nm pumping.

4.1.2 Pumping around 1532 nm. The absorption band for pumping around 1532 nm minimizes the crystal heat load by direct pumping into the emission relevant Stark levels of the $^4I_{13/2}$ manifold. Since this band with a width of 6 nm is narrower than the 1475 nm band, high power laser diodes emitting at that wavelength with line widths of 10–13 nm have reduced absorption efficiencies. This lack of absorption in the wings of the diode emission cannot be changed by the use of longer crystals. Thus fiber laser pumping of this band [3] is better suited for high absorption efficiency.

For pump absorption one can conclude that the intensity drop in the absorption cross-section is mainly due to the temperature induced broadening of the lines. The integral absorption stays nearly constant for broadband pump sources like diodes whenever the pump spectrum is narrower than the absorption band. Then the absorption length can be chosen to be large enough to achieve high absorption efficiencies even at elevated temperatures.

4.2 *Emission*

From the possible emission lines shown in Fig. 5, only the 1617 nm and the 1645 nm emission can be used for efficient laser action, since all emission lines at wavelengths shorter than 1600 nm have strong reabsorption. and from those at wavelengths longer than 1600 nm, the 1617 nm and the 1645 nm emission are the only ones not affected by excited-state absorption to the $^4I_{9/2}$ manifold [13, 14].

A situation equivalent to the ground state manifold is present for the emission lines. The $^4I_{13/2}$ manifold can also be seen as consisting of two sub-manifolds, that are separated by 176 cm^{-1}. Thus the same effect providing enough population for pumping into the $^4I_{15/2}$ manifold is present here, keeping the population of the emission levels high even at elevated temperatures. But the effect is weaker due to the lower separation of the two sub-manifolds compared to that in the ground state manifold. The result is that 43%–37% of the total $^4I_{13/2}$ population is in the starting levels for the emission lines at 300–600 K, respectively.

In the temperature range between 300 and 550 K, a 1.5 and 2 fold decrease in emission cross-section can be seen for the 1617 nm and the 1645 nm emissions, respectively, which is mainly due to increasing linewidths. Re-absorption only increases by about 33% and 66% for these two emission bands in the same temperature range, respectively. But as the terminating levels for the 1617 nm emission are closer to the ground state than the terminating level for the 1645 nm emission, the absolute reabsorption is much higher in the first case and a laser will work more efficiently on the 1645 nm emission lines. It has to be noted that the same sub-manifold effect giving high pump population also reduces the reabsorption for the emission lines, as it ties the center of population to the lower sub-manifold of the $^4I_{15/2}$ manifold. The fact that in the upper sub-manifold of the $^4I_{15/2}$ manifold the terminating level of the 1645 nm emission has three other levels sharing the sub-manifold population, i.e. the partition function is high, also helps in reducing the reabsorption on that terminating level. This results in an increase of thermal population of the lower laser level from only 2% to 6% in the range of 300–600 K.

Concerning laser emission one can conclude that the intensity drop in emission cross-section is also mainly due to the temperature induced broadening of the lines, and since reabsorption is low for the 1645 nm emission, high efficiency laser

action is still possible even at elevated temperatures of around 550 K.

It is interesting to compare the sub-manifold effect in Er^{3+}:YAG with another well known efficient three-level laser medium, Yb^{3+}:YAG. In Yb^{3+}:YAG the ground state manifold has only four levels (0, 565, 612 and 785 cm^{-1}) and no lower sub-manifold can be formed. As the most important 941 nm pump line can only interact with the lowest level, a thermal depopulation of this level from 87% of the total ground state manifold population to 60% at 300–600 K directly affects the pump absorption efficiency. Since there are only four levels in the ground state manifold, i.e. the partition function is low, thermal population of the terminating laser level (612 cm^{-1} in Yb^{3+}:YAG) is higher than in Er^{3+}:YAG at 524 cm^{-1}. The terminating laser level in Yb^{3+}:YAG is thermally populated by 4% at 300 K rising to 14% at 600 K.

4.3 *Predictions on laser efficiency*

Using the simulated cross-sections it was possible to realize a realistic numerical simulation for Er^{3+}:YAG lasers at elevated temperatures [15]. To validate this simulation, the experiments of [2] and [3] were simulated with the parameters given in these references. As can be seen in Fig. 7, the results could be accurately reproduced. In Fig. 8 the optical-to-optical efficiencies for an Er^{3+}:YAG laser equivalent to [3] were calculated for three different setups and various temperatures. The first setup is identical to [3], i.e. especially with a crystal length of 29 mm. The second setup is the same as the first with the output coupler (OC) reflectivity changed to 60%, and the third setup is equivalent to the second, but with a crystal of length 130 mm at 60% OC reflectivity. These high values of outcoupling were chosen to minimize reabsorption. This can be explained by the fact that a laser with high outcoupling will need higher population inversion to increase the round-trip gain compensating the cavity losses above threshold. Thus the population of the lower laser level, i.e. the ground state here, is consequently much lower, which results in lower reabsorption. As a larger outcoupling factor also decreases the intra-cavity field intensity, less laser power will be absorbed by the ground state population.

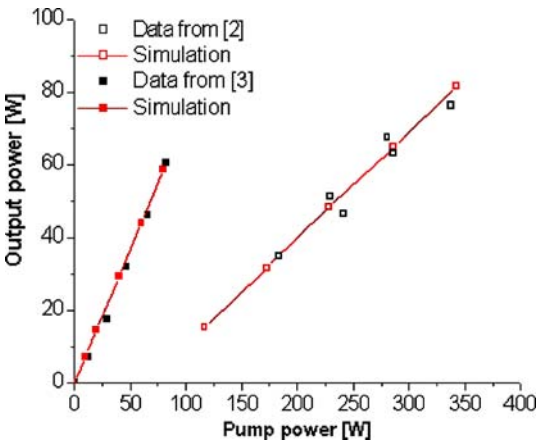

FIGURE 7 Experimental data from [2, 3] and simulation results [15]. Pump power corresponds to the absorbed pump power in [2], and the incident pump power in [3]

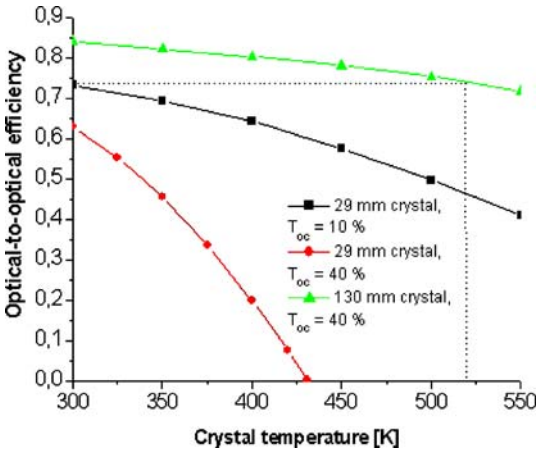

FIGURE 8 Simulated optical-to-optical efficiencies for three different setups [15]

It can be seen that the crystal with 29 mm length has high efficiency at room temperature, that decreases with increasing crystal temperature. This is mainly due to the increasing transparency of the crystal. This setup was optimized with respect to outcoupling, so lowering the OC reflectivity by a factor of 1.5 to 60% causes a decrease in efficiency at 300 K as well as a dramatic decrease in efficiency for higher temperatures according to the numerical calculation. By increasing the crystal length instead, the thermal bleaching in absorption could be minimized and the lower OC reflectivity could be effectively utilized to minimize the increased reabsorption loss due to a lower intra-cavity intensity. For a 130 mm crystal the optical-to-optical efficiency then reaches 84% at 300 K and stays higher than the 300 K efficiency which was reached in the first setup, even at temperatures as high as 520 K. It should be noted that such long crystals would need a pump light guiding structure to allow pumping of the whole crystal with optimum pump intensity.

5 Conclusion

Our investigation of the spectroscopic properties of Er^{3+}:YAG at elevated temperatures shows that efficient laser operation of this laser medium is connected to its special energetic level structure. This influence on the spectra, together with the thermal broadening of the spectral lines, conserves efficient laser operation even at elevated temperatures and even outperforms Yb^{3+}:YAG in terms of pump level population and reabsorption, despite the three-level nature of Er^{3+}:YAG. Thus, less temperature sensitive Er^{3+}:YAG lasers should be possible by specially designing the active medium and cavity, resulting in easier cooling and an increased beam quality with laser architectures in which the active medium may show elevated temperatures.

ACKNOWLEDGEMENTS The authors thank F. Tellkamp (ILP) for technical support.

REFERENCES

1 D. Garbuzov, I. Kudryashov, M. Dubinskii, Appl. Phys. Lett. **86**, 131 115 (2005)
2 D. Garbuzov, I. Kudryashov, M. Dubinskii, Appl. Phys. Lett. **87**, 121 101 (2005)

3 D.Y. Shen, J.K. Sahu, W.A. Clarkson, Opt. Lett. **31**, 754 (2006)
4 M. Dubinskii, N. Ter-Gabrielyan, M. Camargo, G.A. Newburgh, L.D. Merkle, Conf. Lasers and Electro-Optics CLEO 2007, Baltimore, USA, Paper CTuN1
5 S.A. Payne, L.L. Chase, L.K. Smith, W.L. Kway, W.F. Krupke, IEEE J. Quantum Electron. **QE-28**, 2619 (1992)
6 M.G. Beghi, C.E. Bottani, V. Russo, J. Appl. Phys. **87**, 1769 (2000)
7 T. Kushida, Phys. Rev. **185**, 500 (1969)
8 D.E. McCumber, M.D. Sturge, J. Appl. Phys. **34**, 1682 (1963)
9 G.F. Imbush, W.M. Yen, A.L. Shawlow, D.E. McCumber, M.D. Sturge, Phys. Rev. A **133**, 1029 (1964)
10 W.M. Yen, W.C. Scott, A.L. Shawlow, Phys. Rev. A **136**, 271 (1964)
11 D.K. Sardar, W.M. Bradley, J.J. Perez, J.B. Gruber, B. Zandi, J.A. Hutchinson, C.W. Trussel, M.R. Kokta, J. Appl. Phys. **93**, 2602 (2003)
12 M.K. Furtado, R.K. Shori, O.M. Stafsudd, J. Stone-Sundberg, M. Kokta, Advanced Solid-State Photonics 2005, Vienna, Austria, Paper MB10
13 J. Koetke, G. Huber, Appl. Phys. B **61**, 151 (1995)
14 R. Le Boulanger, J.-L. Doualan, S. Girard, J. Margerie, R. Moncorgé, Phys. Rev. B **60**, 11 380 (1999)
15 M. Eichhorn, accepted for publication in IEEE J. Quantum Electron.